The pumice raft-forming 2012 Havre submarine eruption was effusive

Michael Manga[1*], Kristen E. Fauria[1,3], Christina Lin[1], Samuel J. Mitchell[2], Meghan Jones[3], Chris Conway[4], Wim Degruyter[5], Behnaz Hosseini[1], Rebecca Carey[6], Ryan Cahalan[7], Bruce F. Houghton[2], James D.L. White[8], Martin Jutzeler[6], S. Adam Soule[3], Kenichiro Tani[4]

1 Department of Earth and Planetary Science, University of California, Berkeley, CA 94720, USA

2 Department of Geology and Geophysics, University of Hawai'i at Mānoa, 1680 East West Road, Honolulu, HI 96822, USA

3 Woods Hole Oceanographic Institution, Woods Hole, Massachusetts 02543, USA

4 National Museum of Nature and Science, 4-1-1 Amakubo, Tsukuba, Ibaraki 305-0005, Japan

5 School of Earth and Ocean Sciences, Cardiff University, Main Building, Park Place, Cardiff, CF10 3AT, Wales, UK

6 School of Physical Sciences and Centre of Excellence in Ore Deposits (CODES), University of Tasmania, Hobart, TAS 7001, Australia

7 School of Earth and Atmospheric Sciences, Georgia Institute of Technology, 311 Ferst Drive, Atlanta, Georgia 30332, USA

8 Department of Geology, University of Otago, PO Box 56, Dunedin 9054, New Zealand

*Corresponding author, manga@seismo.berkeley.edu

January 17, 2018, revised February 14, 2018

Abstract

A long-standing conceptual model for deep submarine eruptions is that high hydrostatic pressure hinders degassing and acceleration, and suppresses magma fragmentation. The 2012 submarine rhyolite eruption of Havre volcano in the Kermadec arc provided constraints on critical parameters to quantitatively test these concepts. This eruption produced a > 1 km^3 raft of floating pumice and a 0.1 km^3 field of giant (>1 m) pumice clasts distributed down-current from the vent. We address the mechanism of creating these clasts using a model for magma ascent in a conduit. We use water ingestion experiments to address why some clasts float and others sink. We show that at the eruption depth of 900 m, the melt retained enough dissolved water, and hence had a low enough viscosity, that strain-rates were too low to cause brittle fragmentation in the conduit, despite mass discharge rates similar to Plinian eruptions on land. There was still, however, enough exsolved vapor at the vent depth to make the magma buoyant relative to seawater. Buoyant magma was thus extruded into the ocean where it rose, quenched, and fragmented to produce clasts up to several meters in diameter. We show that these large clasts would have floated to the sea surface within minutes, where air could enter pore space, and the fate of clasts is then controlled by the ability to trap gas within their pore space. We show that clasts from the raft retain enough gas to remain afloat whereas fragments from giant pumice collected from the seafloor ingest more water and sink. The pumice raft and the giant pumice seafloor deposit were thus produced during a clast-generating effusive submarine eruption, where fragmentation occurred above the vent, and the subsequent fate of clasts was controlled by their ability to ingest water.

Keywords: submarine eruption; pumice; fragmentation; raft; conduit flow; xray tomography

Highlights:

Havre magma entered the ocean before fragmenting.

Clasts were produced by quenching buoyant magma in the ocean.

Buoyant > 1 m diameter pumice blocks floated to the ocean surface.

Clasts with enough isolated porosity and trapped gas floated in a raft while the rest sank.

1. Introduction

Submarine volcanic eruptions may be fundamentally different from those on land owing to the high hydrostatic pressure provided by the ocean which inhibits degassing and hence magma acceleration and fragmentation. The records of such eruptions are few and our understanding is limited by the challenge in directly witnessing eruption processes and sampling and characterizing the deposits from those eruptions. Indeed, overcoming this biased understanding of volcanic eruptions was highlighted by a National Academies report (National Academies, 2017): "What processes govern the occurrence and dynamics of submarine explosive eruptions"?

Silicic magmas that erupt more than a few hundred meters below sea-level give rise to eruption styles distinct from those on land owing to the contrasting properties of the ambient fluid (water vs air) into which the magmas erupt (Cashman and Fiske, 1991). For example, clasts that erupt at the seafloor are initially buoyant, but ingest water into pore space as they cool (e.g.,

70 Whitham and Sparks, 1986); hence fragmented magma can either rise to the surface to form
71 rafts, or feed submarine density currents if the clasts become waterlogged (Allen and McPhie,
72 2009).
73
74 One distinctive facies of both modern and ancient clastic deposits from submarine silicic
75 eruptions is voluminous deposits of giant (>1 m) pumice clasts (e.g., Kato, 1987; Kano et al.,
76 1996; Kano, 2003; Allen and McPhie, 2009; Allen et al., 2010; Jutzeler et al., 2014). These clasts
77 often have one or more quenched margins with curviplanar joints perpendicular to the cooling
78 surface that suggest they quenched in water (e.g., Wilson and Walker, 1985; Allen et al., 2010;
79 Von Lichtan et al., 2016; Figure 1). Otherwise, submarine pumice vesicularities are similar to
80 those produced in subaerial Plinian eruptions (e.g., Barker et al., 2012) and hence it has been
81 proposed that fragmentation mechanisms are also similar for large (> 1 km^3) submarine
82 equivalents (e.g., Allen and McPhie, 2009; Shea et al., 2013). There are, however, textural
83 differences: pumice clasts from deep submarine eruptions tend to have smaller bubble number
84 densities, lack very small vesicles (<10 μm), and display a narrower range of modal vesicle sizes
85 (Rotella et al., 2015). Clasts have also been proposed to form from buoyant bubbly magma as it
86 exits the vent by "viscous detachment or by the development of cooling joints" (Rotella et al.,
87 2013), an eruption style that would not fit neatly into either the "effusive" or "explosive"
88 categories used to describe subaerial eruptions. Pumice clasts can also form by spallation from a
89 pumiceous carapace on effusive domes (e.g., Cas and Wright, 1987; Kano, 2003; Allen et al.,
90 2010).
91

In July 2012, approximately 1.2 km^3 of rhyolite pumice clasts erupted at a water depth of 900 m from the submarine Havre volcano in the Kermadec volcanic arc (Carey et al., 2014; Figure 1). The majority of the pumiceous material formed a raft of floating clasts that was widely dispersed in the western Pacific Ocean (Jutzeler et al., 2014; Carey et al., 2018). A second clastic product of this eruption is a 0.1 km^3 deposit of giant pumice clasts on the seafloor around the inferred vent. An outstanding question is whether these seafloor giant pumice clasts and raft pumice originated from the same eruptive phase. Though not conclusive, the vesicularities, composition, microtextures (e.g., bubble number densities, crystallinity, microlite mineralogy), and macrotextures (e.g., banding), are similar as is their primary axis of dispersal (Carey et al., 2018). If the raft and seafloor pumice did originate from the same eruptive episode, their different fate, i.e., whether they floated or sank, thus requires seafloor giant pumice to ingest water more effectively than clasts that were transported into the raft.

Here we use a model for magma ascent, constrained by estimates of the eruption rate for the pumice raft and a variety of measurements on erupted materials, to show that buoyant magma reached the seafloor prior to fragmenting. We then investigate how pumice clasts from the raft and seafloor ingest water as they cool and find that seafloor pumice ingest water more efficiently by trapping very little gas. We thus infer that vesicular coherent magma extruded into the ocean. The magma quenched and fragmented non-explosively to form the pumice clasts that then either remained afloat because they retained enough gas or, if they waterlogged, settled to the seafloor.

2. Methods

115 **2.1 Conduit model**

116

117 Magma ascent is simulated using a one-dimensional two-phase model for steady flow, modified
118 from Degruyter et al. (2012) and Kozono and Koyaguchi (2009). Pressure at the vent is 9 MPa
119 corresponding to a water depth of 900 m. The conduit length is 8.1 km with a pressure at its base
120 of 200 MPa. Crystallinity is 5% (Carey et al., 2018) and crystals do not grow or nucleate during
121 ascent. The effects of crystals and bubbles on viscosity are based on the models of Costa (2005)
122 and Llewellin and Manga (2005), respectively (supplement S1). Water content in the melt is 5.8
123 weight % based on 16 plagioclase-hosted melt inclusions from a seafloor giant pumice clast
124 (supplement S2). Number density of bubbles is 10^{14} m^{-3} (Rotella et al., 2015), high enough that
125 we can assume equilibrium bubble growth (Gonnermann and Manga, 2005); we obtain similar
126 ascent rates for number densities 100 times lower and higher. The effects of temperature and
127 dissolved water on viscosity are computed using Giordano et al. (2008) and the measured
128 composition (supplement S3) and water content. Temperature is set to 850 ± 20 °C based on cpx-
129 opx Fe-Mg exchange (Putirka, 2008) in ten measured cpx and opx compositions. Magma can
130 fragment in the conduit if the strain-rate $\dot{\gamma}$ exceeds a critical value (e.g., Papale, 1999)

131 $$\dot{\gamma} > 10^{-2} G/\mu \,, \qquad (1)$$

132 where $G = 10^{10}$ Pa is the shear modulus (e.g., Simmons, 1998) and μ is the melt viscosity. We
133 compute both the strain-rate at the conduit walls and the elongation strain-rate in the center of the
134 conduit.

135

136 It is important to recognize that in addition to uncertainties in magma properties there are
137 also model assumptions that affect strain-rates, ascent velocity, and vesicularity at the vent. For

example, the ascending magma is assumed to be isothermal and Newtonian, we neglect viscous heating and shear localization in the magma, and we do not permit non-equilibrium bubble growth. We also use a geometrically idealized conduit shape. In addition, we assume that at any given depth the bubble size is uniform and use this bubble size to compute a permeability. There are, however, bubbles much larger than the mean size which, owing to the nonlinearity of permeability-bubble size relationships, could lead to higher permeability and more outgassing.

2.2 Floatation experiments

To determine the propensity for Havre pumice clasts to remain afloat after reaching the raft at the ocean surface, we conducted 11 experiments in which we measured the amount of liquid water and trapped gas within cm-sized clasts from the Havre raft (7 samples) and fragments of seafloor giant pumice (4 samples). We heated dry raft clasts and giant pumice fragments to a range of temperatures up to 700°C and placed them on the water surface for ten minutes. We then rapidly encased the clasts in wax – to minimize further changes in the distribution of internal fluids – and imaged the clasts at 1.22 μm resolution using X-ray computed microtomography (XRT) with 30 keV monochromatic X-rays. To enhance the absorption contrast between the water and glass, we used a 13 weight% potassium iodide solution. Additional imaging details are provided in supplement S4. From the XRT images, we identified the volumetric content of glass, liquid water, and trapped gas within the clasts using machine learning algorithms to segment these three phases (Fauria et al., 2017).

To further quantify pumice floatation dynamics, we measured the floatation time of room temperature raft and seafloor clasts. To measure floatation times, we placed dry and ambient temperature clasts in water and noted the time at which they sank. Before the experiments, we cleaned the clasts in an ultrasonicator for ~10 mins and then dried them. Once the experiments were initiated, we monitored the clasts with a camera and noted the time at which the clasts sank to the nearest minute. If clasts continued to float after the first six months of the experiments, we stopped monitoring with a camera and began checking on the clasts approximately daily and then weekly once the experiments progressed past the first year.

We measured clast weight before and after the experiments. For a subset of the clasts, primarily the seafloor clasts, we measured clast volume using photogrammetry. Specifically, we took 100-180 photographs per clast using a Canon DSLR camera with an extension tube. We processed the images and constructed volume models (Poisson surface reconstructions) using VisualSFM and MeshLab softwares. In cases where the clasts were too small to accurately measure volume using photogrammetry, we estimate pumice volume using pumice mass assuming a clast porosity of 83% (Carey et al., 2018).

2.3 Isolated porosity

Differences in isolated porosity between the raft and seafloor samples are unresolvable in the XRT scans. We thus use helium pycnometry to quantify the connected and unconnected pore space. Samples were cored, washed, dried, and weighed. The volume of the cylindrical cores was calculated based on the mean of 10 measurements of the sample diameter and height. The

183 volume of the solid phase and isolated porosity was measured using a He-pycnometer at the
184 University of Oregon using methods described in Giachetti et al. (2010). The pycnometry
185 measurements and bulk volume were used to calculate the connected porosity. One seafloor
186 sample and one raft sample were crushed, weighed, and analyzed using He-pycnometry in order
187 to determine the solid density. The bulk vesicularity was calculated from the solid density, bulk
188 volume, and bulk density. The isolated vesicularity was calculated from the difference between
189 the bulk vesicularity and connected vesicularity.
190
191 **3. Results**
192
193 Figure 2 shows how ascent velocity, mean bubble size, melt viscosity, and vesicularity
194 vary with depth in the conduit for conduit radii of 3, 21 and 33 m. The corresponding mass
195 eruption rates are 4.2×10^3, 1.0×10^7 and 6.2×10^7 kg/s respectively. This model reproduces the
196 observed vesicularity of about 80-90 % and modal vesicle size (Rotella et al., 2015; Carey et al.,
197 2018). A conduit radius of 21 m leads to a mass eruption rate similar to the time-averaged value
198 inferred from the volume of the pumice raft and the estimated duration of the raft-forming stage
199 of the eruption, 9×10^6 kg/s (Carey et al., 2018). For this eruption rate, Figure 2b shows that the
200 gas and melt remain coupled and there is negligible outgassing during ascent. The model does
201 not account for any further modification of vesicularity of clasts after they enter the ocean.
202
203 There are uncertainties in all model parameters including, critically, those that affect
204 viscosity: water content and temperature. However, the main conclusions are not sensitive to
205 reasonable ranges in these parameters. For example, if we reduce the water content to 5% and

206 temperature to 820 °C, even for an eruption rate an order of magnitude greater than inferred,
207 1×10^8 kg/s, the strain-rate is still a factor of 5 too low to cause melt to fragment based on
208 equation (1).
209
210 Figure 3 shows that reheated (> 500°C) Havre raft pumice can retain enough gas to
211 remain buoyant. By comparison, fragments from the seafloor giant pumice are almost fully
212 saturated (< 0.05 volume fraction gas) after they are reheated above 500°C and placed on the
213 water surface. The results from these experiments demonstrate that hot Havre seafloor giant
214 pumice draw in considerably more water than raft pumice. In raft pumice, some of the gas is
215 trapped by the infiltrating water (red arrow), but there is also a significant amount of
216 unconnected porosity (isolated bubbles). This difference is further highlighted by the pycnometry
217 measurements. Figure 4 shows the connected and unconnected porosity analysis and reveals that
218 seafloor giant pumice has fully connected porosity whereas raft pumice always contains isolated
219 bubbles. These differences may be documenting samples from different parts of the conduit, or
220 samples that experienced different and continued vesiculation histories in the water column. A
221 thorough analysis of textures from raft and seafloor samples may reveal not only why some
222 clasts float, but provide further insights into ascent processes in the conduit and water column.
223
224 Figure 5 shows clast volume versus floatation time. We identify clasts that were still
225 floating at the time of manuscript submission with red outlines. We find that floatation time
226 increases with clast size and that raft pumice float orders of magnitude longer than seafloor
227 pumice. We compare pumice floatation times to a diffusion model for pumice floatation from
228 Fauria et al. (2017). The model predicts that floatation time scales as

$$\tau = \frac{4R^2}{D_a \theta^2}, \quad (2)$$

where τ is time, $2R$ is clast diameter, $D_a = 1.9 \times 10^{-9}$ m^2/s is air-water diffusivity (Fauria et al., 2017), and θ is the fraction of pore space containing liquid water. The shaded region in Figure 5 shows predictions of equation (2) with θ between 0.1 and 0.5. Seafloor clasts match the diffusion model prediction while raft pumice float much longer than predicted and, indeed, have yet to sink. The presence of isolated bubbles (Figure 4) may explain why cold raft pumice float much longer than theoretical models predict.

4. Discussion

We now address in order three basic questions about the 2012 Havre eruption. Where and why did the magma fragment? What processes form meter-sized clasts? Why do some pumice clasts float (raft pumice) and others sink (seafloor giant pumice)?

4.1 Fragmentation

From the conduit model, strain rates never become large enough to cause brittle fragmentation within the conduit of the Havre eruption. Instead, at 86% vesicularity, the erupting magma is less dense than sea water and hence will continue to rise above the vent rather than creating a dome. What processes then create the pumice? We do not favor buoyant detachment of blebs by gravitational instabilities, one mechanism suggested for example by Rotella et al. (2013),

because the separation of blebs is slow compared to the inferred extrusion velocity for the Havre eruption and we did not see fluidal-shaped clasts either near the vent or in samples from the raft. For a bleb of length l and radius r buoyantly rising above the extruding magma, the velocity $dl/dt \approx \frac{(\rho_w - \rho_c) g r^2}{\mu} \ln (l/r)$, where ρ_c is clast density, ρ_w is water density, and g is gravity (Olson and Singer, 1985). This is a Stokes flow scaling, appropriate because the magma viscosity controls extrusion prior to fragmentation. Choosing $l = 2r$ for equant bleb, $\mu = 5 \times 10^6$ Pa s (Figure 2), $\rho_w - \rho_c = 500$ kg m^{-3} (Rotella et al., 2015; Carey et al., 2018), and l=5 m, we obtain an ascent speed of 4 cm/s, much less than the velocity at the vent of 14 m/s (figure 2). The melt is so viscous that ductile processes are too slow to produce clasts.

Instead, we suggest that the surface of extruded magma will quench in the ocean, producing a network of cracks perpendicular to the magma surface. Highly vesicular magma is prone to quench fragmentation and the temperature difference between magma and seawater is sufficient to create cracks (van Otterloo et al., 2015), possibly aided by continued vesiculation. Crack propagation speeds can be tens to hundreds of meters per second (van Oterloo et al., 2015) so that a large volume of fragmented debris can be produced very quickly. Although a range of fragment sizes will be produced, they will not be able to separate and rise unless they can also float upwards fast enough from the extruding magma. Smaller fragments may weld together, or may break off larger clasts or the side of the extruding spine of magma if the spine extends above the vent.

4.2 Separating pumice from extruding magma

The terminal rise speed U of clasts produced by quenching and surrounded by water, idealized here as spherical with radius R, is

$$U = \sqrt{\frac{8(\rho_w - \rho_c)gR}{3\rho_w C_D}} \quad . \qquad (3)$$

Given the very high Reynolds number (~10^7), the drag coefficient C_D is approximately 0.3 (e.g., Batchelor, 1967). Equation (2) also neglects entrainment by the buoyant warm water heated by the clasts, which would increase velocity. With a conduit radius of 21 m the vent velocity is 14 m/s (Figure 2), and clasts with R>4.5 m will rise faster than the extrusion speed, at least before they ingest water. Exit velocity is inversely related to conduit radius owing to mass conservation. If the vent widens by 40% at the seafloor, the minimum radius R for detachment decreases to 1.2 m. There are uncertainties in both the mass eruption rate that constrains the exit velocity and the parameters that affect the minimum size of clasts computed from equation (3), but predicted meter-sized clasts are similar to typical sizes of the giant pumice on the seafloor, averaging 1-1.6 m near the vent and increasing with dispersal distance (Carey et al., 2018).

4.3 Reaching the sea surface

Clasts that detach from the extruded magma will rise through the ocean until they saturate with water. Once saturated, clasts will become negatively buoyant and sink to the seafloor. For meter-sized clasts, water ingestion is limited not by permeability but by the ability of water vapor in the clast to cool, condense and draw in liquid (appendix A). As cooling is slower than permeable flow, the rate of heat loss from the interior of the pumice will determine the time to saturation. To compute the evolution of clast density through water ingestion, and hence their ascent through the ocean, we model the cooling, condensation, and thus flow of liquid water into

297 spherically symmetric clasts using experimentally measured rates of heat loss, and compute the
298 rise speed of the clasts using equation (3) from the time-evolving mean clast density (assuming
299 fully connected porosity). We allow gas in the clasts to expand as the ambient pressure decreases
300 (appendix B) which is significant because water vapor density is > 15 kg/m^3 at 900 m water
301 depth and ~ 1 kg/m^3 at the surface. Additional joints within clasts would enhance water ingestion
302 and cooling beyond what we model. We neglect any possible further vesiculation within clasts as
303 they rise through the ocean. Although clasts may remain hot as they ascend and can continue to
304 exsolve water, vesicles need not grow if the pore space is connected to permit gas leakage to the
305 ocean (e.g., Kueppers et al., 2012). Figure 6 shows the time required for clasts of different
306 vesicularities to reach the ocean surface before they become negatively buoyant in water. Meter-
307 sized clasts, such as the seafloor giant pumice, are expected to reach the raft at the ocean surface
308 and will have ingested little water. The initial sizes of raft pumice are not known, but Figure 6
309 suggests that a minimum size of about one meter is required for clasts to reach the surface.
310
311 *4.4 To sink or float?*
312
313 The long-term fate of floating pumice on the sea surface depends on their ability to ingest
314 additional water as they float. The ascent model predicts that there is virtually no liquid in meter-
315 sized and larger clasts as they reach the sea surface owing to the expansion of vapor in the clasts
316 during ascent (appendix B). However, the seafloor deposit of giant pumice comprises clasts up to
317 9 m in diameter (Carey et al., 2018). Some of those may include pumices that are large enough to
318 reach the sea surface, but are trapped underneath floating pumice and remain fully surrounded by
319 water, in which case we would expect them to sink once the water vapor cools and condenses

(Allen et al., 2008). Others must have reached the sea surface and subsequently saturated with water.

Once pumice reaches the sea surface, we expect air to replace most of the water vapor in the pore space because gas diffusion and exchange is rapid, and is further enhanced as clasts crack or break. Air-filled pumice is known to float much longer (e.g., Whitham and Sparks, 1986; Manville et al., 1989; Dufek et al.., 2007; Jutzeler et al., 2017) than the time it takes for porous flow to allow water to infiltrate (Vella and Huppert, 2007). Instead, the ability of clasts to float is controlled by the propensity of the infiltrating water to trap gas bubbles within the pore space and/or the presence of isolated vesicles. If enough gas is trapped during infiltration of water, the clasts will float until this gas diffuses through the water and out of the clast (Fauria et al., 2017).

The difference in isolated and connected porosity can partially explain the propensity for raft pumice to float, however, additional gas trapping is required for most clasts (Figure 4). Our experiments confirm that fragments of seafloor giant pumice ingest more water and trap less gas than raft pumice, and hence more rapidly become negatively buoyant. The presence of elongate "tube" vesicles in some seafloor pumice has further implications for why some clasts sink preferentially to others. The elongate structure, high connectivity and anisotropic permeability of such vesicles would permit rapid clast saturation and subsequent sinking to the seafloor (Wright et al., 2006). The diversity of these textures within pumice deserves more detailed microtextural analysis.

We thus propose that what separates pumice into the raft is their ability to trap gas and the presence of isolated vesicles; clasts that cannot retain enough gas sink. Those that trap gas and/or have sufficient isolated vesicles float. Presumably the difference in gas trapping results from differences in topology of the pore space such as the number of dead-end pores. We could not, however, identify any key differences in our images. We note several caveats, however. First, we are not able to do experiments on meter-sized raft or seafloor clasts owing to the lack of intact samples and our inability to measure and image the infiltration at such large scales. We thus assume that the smaller fragments we imaged are representative of the larger clasts from their respective units. Second, we do experiments on quenched samples, whereas the vesicularity and texture of the pumice may evolve during quenching and also after their initial fragmentation. Larger clasts should take longer to ingest water, explaining why seafloor pumice clast size increases with distance from the vent (Carey et al., 2018).

4.5 The effusive eruption of Havre

The raft-forming Havre eruption was not explosive in the same manner as subaerial pumice clast-forming eruptions. This submarine style of pumice-generating eruption requires an eruption depth that is not-too-deep and not-too-shallow (Figure 7). In deeper water, with the critical depth depending on the water content of the melt, the magma will not be buoyant and will form a lava flow or dome (Figure 7c). In shallower water, the melt viscosity will be higher owing to greater gas exsolution and the magma may undergo brittle fragmentation in the conduit (Figure 7a). For the Havre mass eruption rate, composition, and water content, a vent depth of 2.8 km will lead to the erupting magma being denser than seawater (1030 kg/m^3), and a vent shallower

than 290 m will allow the magma to fragment in the conduit (21 m radius) assuming that the criterion given by equation (1) is accurate. It is worth noting that the Taupo eruption which also produced giant pumice fragments, and was dominated by Plinian-phreatoplinian explosions and magmatic fragmentation in the conduit, occurred in water depths that were never more than 200 m (Wilson and Walker, 1985; Houghton et al., 2003). Mass discharge rate also matters because low ascent rates enable outgassing. For example, at Havre multiple lava domes with low-to-moderate vesicularity extruded in 2012 at the same water depth as the vent that produced the giant pumice clasts. At Sumisu Dome C in the Sumisu Dome Complex, Izu Bonin Arc, Japan, silicic pumiceous dome carapaces at 1100-1300 mbsl have high vesicularity, between 60 – 85%, and did not produce a clastic deposit (Allen et al., 2010).

The 2012 eruption that produced the pumice raft partly conforms to the eruption style proposed by Rotella et al. (2013) in which bubbly magma enters the ocean and clasts detach from the extruding magma; we favor "cooling joints" and other mechanical stresses over "viscous detachment" for Havre because the effusion velocity is so high and because we lack evidence for any wholly or partly bleb-shaped clasts; ductile processes, however, may be important for creating floating clasts from less viscous magmas (e.g., Kueppers et al., 2012). As noted by others (e.g., Cas and Giordano, 2014; Allen and McPhie, 2009; White et al. 2015), terminology such as explosive and effusive, developed for subaerial eruptions and their deposits, may not translate well to the submarine realm where high hydrostatic pressure and the cooling effects of liquid water can modulate fragmentation.

Given that submarine giant pumice deposits are common products of historical eruptions and well documented in the rock record (Reynolds et al., 1980; Kano et al., 1996; Risso et al., 2002; McPhie and Allen, 2003; Kano, 2003; Allen and McPhie, 2009; Allen et al., 2010; Jutzeler et al., 2014; Von Lichtan et al., 2016), we infer that the 2012 Havre eruption may be an example of a relatively common style of deep submarine volcanic eruption. Modern intra-oceanic arcs, such as the Kermadec, Izu, Bonin, Mariana, and South Sandwich arcs contain many deep submarine silicic volcanoes, and similar eruptions may be common.

5. Conclusions

The 2012 pumice raft-forming eruption was produced from a vent that extruded buoyant vesicular rhyolite into the sea at speeds > 10 m/s. This lava fragmented by quenching in the ocean to produce three subpopulations of clasts. Large clasts (> 1 m) rose to the sea surface without ingesting enough water to sink. Those large clasts with sufficient isolated vesicles and/or trapped gas remained afloat in the raft. Large clasts that did not retain enough gas, and those that were trapped beneath the pumice raft, sank to create the seafloor giant pumice. Smaller clasts would not have reached the surface, ingesting water quickly and settling close to the vent, or were transported by currents if small enough.

The eruption style documented at Havre may be dominant for submarine silicic eruptions, as most submarine vents are at depths greater than a few hundred meters. Voluminous deposits of giant pumice clasts are a product, and thus an indicator, of large, deep silicic effusive eruptions. This eruption style can partition most of the mass into distal and global ocean basins, which has

411 implications for how we interpret past events and may ultimately lead to a re-evaluation of the
412 volumes and magnitudes of submarine eruptions in the past.
413
414 **Acknowledgements**: MM, KF, CL and BH are supported by NSF 1447559. SM and BH are
415 supported by NSF 1357443. RJC was funded by the Australian Research Council
416 (DP110102196, DE150101190). AS is supported by NSF 1357216. MJ is supported by a
417 National Defense Science and Engineering Graduation Fellowship. XRT was enabled by the
418 Lawrence Berkeley National Lab Advanced Light source, beamline 8.3.2, and guidance from
419 Dula Parkinson. Additional support was provided by the Marsden fund and the 2017 Student
420 Mentoring and Research Teams (SMART) Program, Graduate Division, University of
421 California, Berkeley. Fumihiko Ikegami created Figure 1d. Brian Monteleone provided
422 assistance in SIMS analysis of melt inclusions at the Northeast National Ion Microprobe Facility.
423 Melissa Rotella provided the raft clasts using in the floatation experiments. Thomas Giachetti
424 provided assistance with He-pycnometry. We thank Tushar Mittal, Dan Fornari, Jocelyn McPhie,
425 Ray Cas and an anonymous reviewer for comments, and the rest of the MESH team, ROV and
426 AUV operators, and Roger Revelle crew for making this science possible.
427
428 **Author contributions**. MM and WD modeled magma ascent. KF and CL perfomed the
429 ingestion experiments and analysis. RC and SM measured volatiles. CC measured composition.
430 KF and BH did the floatation experiments. MJ measured porosity. KF and MM developed the
431 clast ascent and ingestion model. All authors contributed to sample collection, interpretation and
432 writing.
433

Appendix

A. Why ingestion is not likely to be limited by permeability for large clasts

As the interior of vapor-filled pumice cools, vapor condenses and draws in liquid water. Whether heat loss or permeability limits this ingestion of liquid depends on the ability of a clast to lose heat compared to the ability of liquid to flow into the clast – the slowest process will govern liquid ingestion.

The condensation of vapor and heat loss from the clast is similar to the classic Stefan problem except that advection of heat by liquid water drawn into the clast may dominate the heat transport. An energy balance at the vapor-liquid interface balances the conductive transport across that interface with the latent heat released

$$-\kappa \frac{dT}{dx} = \rho_s \phi L u \quad (\mathrm{A.1})$$

where u is the fluid velocity, L the latent heat, $\rho_s$is the density of steam, ϕ is porosity, T is temperature, κ is the thermal conductivity of the liquid-saturated clast, and x is position. The temperature distribution within the liquid-saturated part of the clast that determines the left-hand side of equation (A.1) depends on u, and we use the solution for steady-state advective-diffusion problem from Bredehoeft and Papadopulos (1965)

$$\frac{T(x) - T_a}{T_s - T_a} = \frac{e^{\beta x/a} - 1}{e^{\beta} - 1} \quad (\mathrm{A.2})$$

where $\beta = ua/D$ is a dimensionless Peclet number (ratio of advection to diffusion of heat), where D is the thermal diffusivity of the liquid-saturated clast, a is the distance from the clast surface to the steam-liquid interface, and T_a and T_s are the temperatures of the ambient water and steam-liquid interface, respectively. The solution for the infiltration speed can be obtained by solving equations (A.1) and (A.2)

$$u = \frac{D}{a}\ln\left[1 + \frac{\kappa(T_s - T_a)}{\rho_s \phi L D}\right] \quad \text{(A. 3)}$$

If permeability limits the infiltration speed of water, a lower bound on the velocity is given by Darcy's law assuming buoyancy controls infiltration

$$u > \frac{k\rho_w g}{\mu_w \phi} \quad \text{(A. 4)}$$

where k is permeability, and μ_w is the viscosity of water. We use > because we neglect the additional (and likely much larger) pressure gradients from gas contraction and capillary forces that would further increase u.

Whether heat loss controls infiltration (equation A.3) or permeable flow (equation A.4) depends on which is larger – the slowest velocity is rate-limiting. Permeability is not limiting if

$$k > \frac{\mu_w \phi D}{a\rho_w g}\ln\left[1 + \frac{\kappa(T_s - T_a)}{\rho_s \phi L D}\right] \quad \text{(A. 5)}$$

Using $D = D_w\phi + D_r(1-\phi) = 2.5 \times 10^{-7}$ m^2/s for $\phi = 0.8$, where D_w and D_r are the diffusivities of water and glass, respectively (Bagdassarov et al., 1994), $\kappa = 2$ Wm^{-1}K^{-1} , and conditions at the ocean surface ($T_s - T_a$=100 ^{o}C, ρ_s=1 kg/m^3), we find that cooling is limiting provided $k > 1.2 \times 10^{-13}$ m^2 for a clast with a = 1 m. Permeability of pumice is generally larger

than this value, typically > 10^{-12} m^2 for vesicularities of 70-80% (e.g., Rust and Cashman, 2004; Mueller et al., 2005; Burgisser et al., 2017; Colombier et al., 2017; Gonnermann et al., 2018). Note that the value of k from equation (A.5) is an upper bound because we ignore additional pressure gradients driving water into the clast in equation (A.4) and densities and temperature difference at greater depths decrease the velocity predicted by equation (A.2). The model also neglects any interfacial instabilities that might enhance infiltration or change effective diffusivities (e.g., Randolph-Flagg et al., 2017).

B. Cooling, ingestion and ascent model

We model the density evolution and rise of hot and initially water vapor-saturated clasts. Clast density evolves due to internal gas decompression, contraction of vapor by cooling and condensation, and from liquid water infiltration. We assume that the clast vesicularity does not change due to volatile exsolution after clasts form. By coupling a model for clast density evolution to a model for clast rise speed (equation 3), we can estimate the time it takes clasts of varying sizes and vesicularities to reach the ocean surface from a depth of 900 m (Figure 6).

Consider a clast that is entirely filled with water vapor such that $f = 1$, where f is the fraction of pore space filled with water vapor. The clast has vesicularity, ϕ, initial temperature, T, diameter, D, and originates from a depth of 900 m. We assume an initial temperature of 850°C and calculate the initial density ρ_s, mass, m_s, and specific enthalpy, H, and total enthalpy, H_T, of internal the water vapor using a thermodynamic look-up table (IAPWS IF-97, XSteam;

501 Holmgren, 2006). We assume that the internal steam is fully coupled to the clast and cannot flow
502 out unless the volume of steam exceeds the internal volume of the clast pore space. We calculate
503 clast density as

504 $$\rho_c = \rho_r(1-\phi) + \rho_s\phi f + \rho_w\phi(1-f) \qquad \text{(B.1)}.$$

505

506 where the subscripts *r* and *w* stand for rock and liquid water. Clast density changes primarily as a
507 function of the volume of internal water vapor, which in turn is affected by cooling and
508 decompression. Clasts lose thermal energy through cooling according to

509 $$\frac{dH_T}{dt} = -qFS \qquad \text{(B.2)},$$

510 where q is an average rate of heat loss that was measured experimentally to be approximately 7.5
511 W cm^{-2} for initially air-filled pumice in water (Fauria, 2017), S is clast surface area, and F is a
512 factor that describes the partitioning of latent heat within the water vapor and sensible heat
513 within the glass. The ratio of sensible to latent heat in the clasts is characterized by the Stefan
514 number

515 $$\mathrm{St} = \frac{\Delta T c_p}{\phi L} \sim 1 \qquad \text{(B.3)},$$

516 where ΔT, is the temperature difference between the initial clast temperature and ambient water,
517 c_p is the heat capacity of the glass, and L is the latent heat of vaporization. We define

518 $$F = \frac{\phi L}{\Delta T c_p + \phi L} \qquad \text{(B.4)}.$$

519 The factor F accounts for sensible heat loss from the glass. That is, not all heat is drawn out of
520 the internal water vapor, rather a proportion of cooling affects the glass. For an 850°C clast, we
521 estimate $F \sim 0.5$. We find that precise value for F does not affect the calculated clast rise speeds,
522 but is important for determining the minimum clast size that can reach the surface.

We calculate clast rise speeds as a function of clast density and size using equation (3). Clast rise distance Z through the water volume is

$$Z = \int U dt. \qquad (B.5)$$

We relate depth h to pressure according to $P = \rho_w g h$. At each new depth we calculate the density and volume, V_s, of the internal water vapor as a function of pressure and specific enthalpy using a thermodynamic lookup table (XSteam; Holmgren, 2006). Internal water vapor can expand as clasts rise through the water column, and contract due to cooling. The volume fraction of pore space filled with water vapor is

$$f = \frac{V_s}{\phi V_c}. \quad (B.6)$$

If the net effects of cooling, decompression, and gas expansion make the volume of internal water vapor exceed the volume of the pore space such that $f > 1$, we let all excess water vapor exit the pore space and set $f = 1$. We define the excess water vapor as $E_x = f - 1$. We write the change in water vapor mass and total enthalpy due to vapor escape from the clast as

$$\Delta m_i = -E_x V_c \phi \rho_{s,} \quad (B.7)$$

$$\Delta H_T = -\Delta m_i H. \quad (B.8)$$

In contrast, cooling can make contraction and condensation exceed decompression effects such that $f < 1$. If this is the case, we allow water liquid water to enter to pore space vacated by steam due to condensation (e.g., Fauria, 2017), but does not decrease the clast's enthalpy. Equation

546 (B.1) demonstrates, however, how ingested water increases clast density and thereby affects rise
547 speed, decompression rates, and clast fate.
548
549 We solve equations (3) and (B.1-8) using a first order finite difference scheme. The model ends
550 when a clast either reaches the ocean surface or becomes neutrally buoyant due to vapor
551 condensation and water ingestion. Figure 4 shows how clast size affects rise time to the surface
552 and the minimum clast sizes required to reach the surface from a depth of 900 m. Below these
553 minimum clast sizes, cooling results in vapor condensation and buoyancy reversal before a clast
554 can reach the surface (Figure 4).
555
556 Many of the assumptions in equations (B.2-B.8) and approximations needed to develop this
557 model could, in principle, be relaxed with a full 3D multiphase flow model that includes gas
558 exsolution from the melt and mass, momentum and energy exchange with the surrounding water,
559 and the presence of unconnected porosity (Figure 4). The model used here also neglects the
560 buoyant ascent of warm water that would entrain clasts. A model that couples clast-scale
561 processes and large scale dynamics may improve the accuracy of calculations of the fate of clasts
562 and may reveal new and neglected processes.
563
564 If there is unconnected porosity, and all the connected porosity fills with liquid water, the
565 unconnected porosity is able to keep clasts floating if

566 $$\phi_u = \frac{(\rho_r - \rho_w)}{(\rho_w - \rho_s)}(1 - \phi_t) \quad \text{(B.9)}$$

567 where the subscripts on density are as before and *u* and *t* indicate unconnected and total porosity,
568 respectively.

569

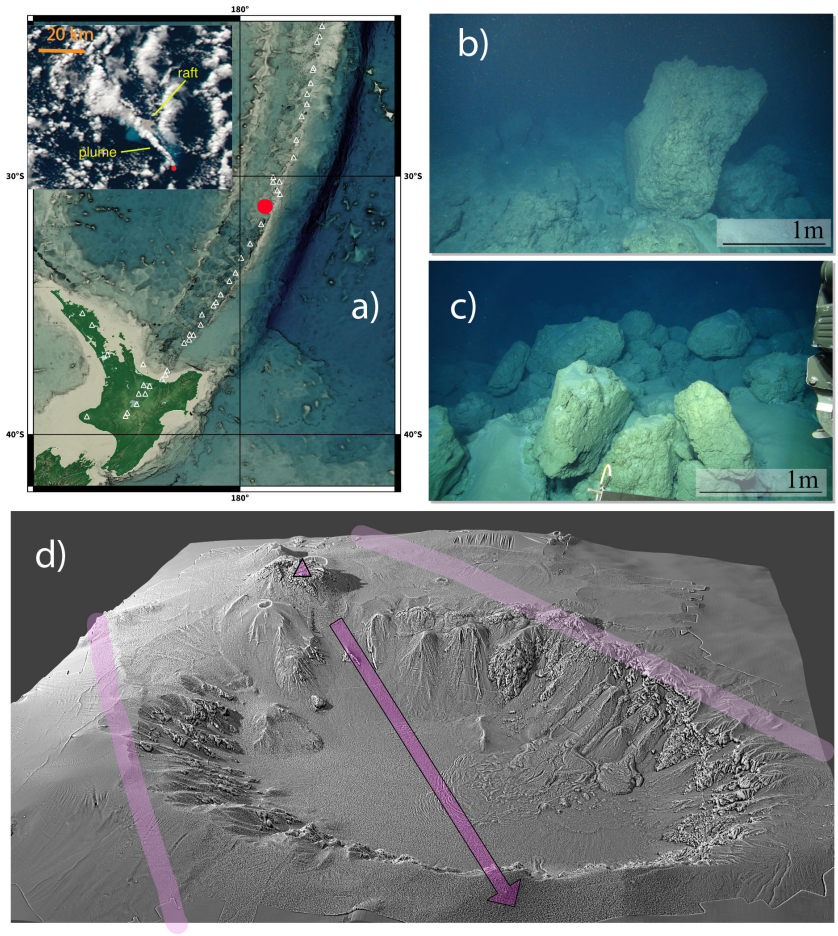

Figure 1: a) Location of the Havre volcano (red circle) in the Kermadec arc. Inset shows the raft and plume on 19 July, 01:26 UTC. Inset scale bar is 20 km long. Plume and raft show the transport direction to the northwest. Example seafloor giant pumice clasts showing curviplanar surfaces (b) and typical deposit (c). d) Shaded relief map showing the vent location (triangle) at a depth of 900 m; arrow shows the dispersal axis of seafloor giant pumice (the same as the transport direction in a), and the light purple lines bound the region containing those clasts. Caldera is 4.5 by 5 km in size. Viewing direction is looking south.

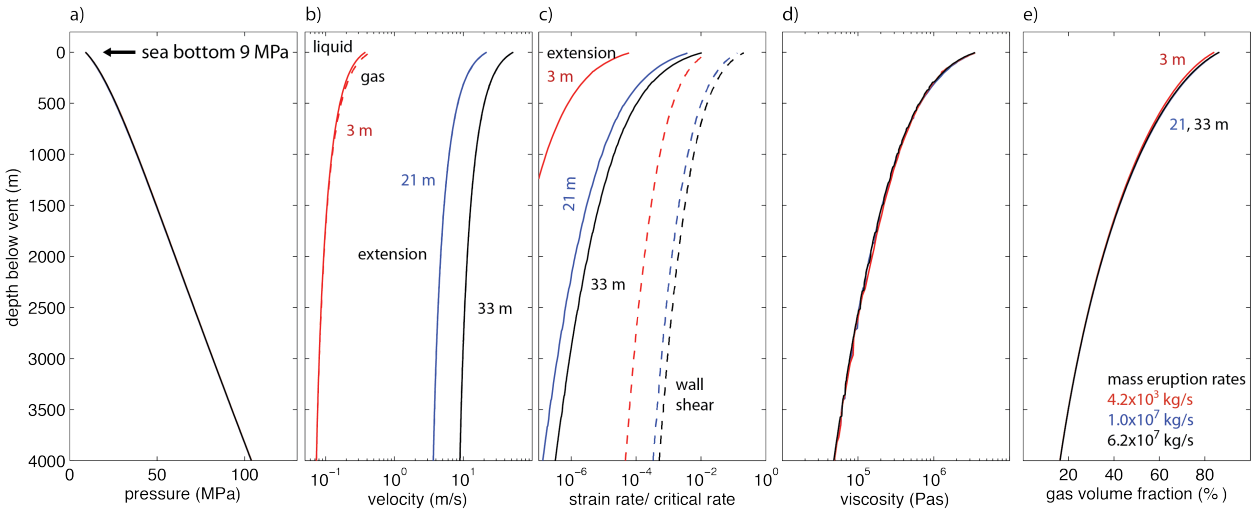

Figure 2: Magma ascent and gas escape, computed using the steady one-dimensional model of Degruyter et al. (2012) with melt properties for the Havre 2012 rhyolite eruption, showing how pressure (a), melt (solid curves) and gas (dashed curves) velocities (b), strain-rate relative to that needed to cause brittle fragmentation (c), magma viscosity (d), and vesicularity (e) varies with depth below the seafloor. Three conduit radii are assumed, 3, 21 and 33 m. Only the upper 4 km of the conduit are shown. Additional parameters: the percolation threshold for gas flow through the magma is zero, tortuosity factor is 3, bubble throat to radius ratio is 0.31, and the friction coefficient for gas flow through the magma is 10 (supplement S1 for details).

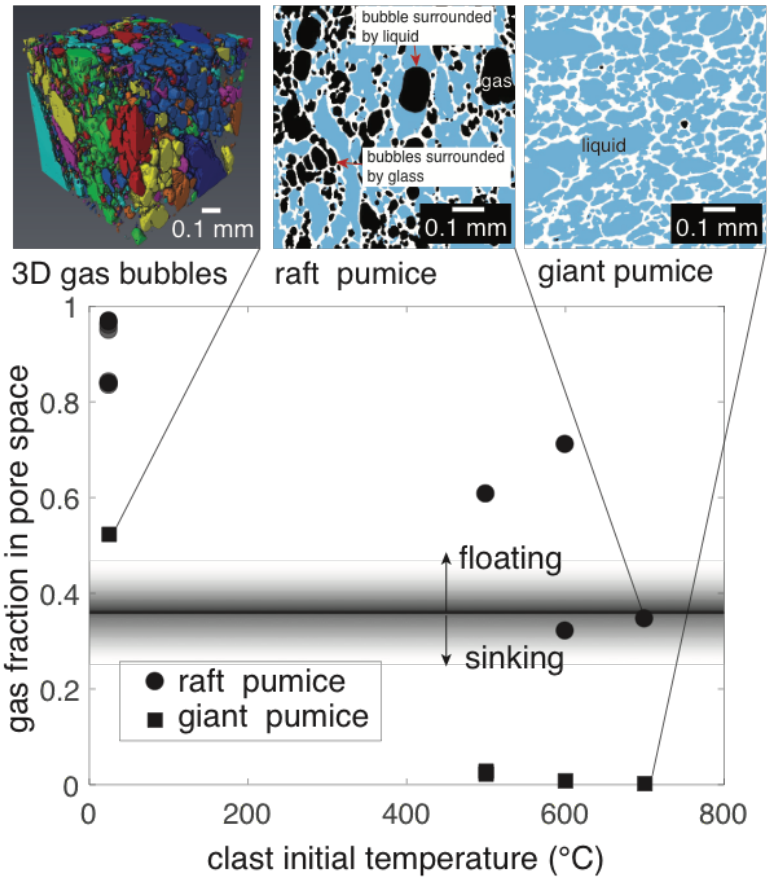

593 .

594

595 **Figure 3**: Initially hot pumice ingests more water than cold pumice, and giant pumice fragments
596 (unknown locations within the larger clast) recovered from the seafloor ingest more water than
597 pumice from the raft. A different pumice clast is used for each experiment and hence data point.
598 The horizontal line shows the trapped gas fraction needed to keep a clast with a vesicularity of
599 80% buoyant. The two images on the upper right are 2D slices through their 3D images showing
600 the distribution of glass (white), trapped gas (black), and liquid water (blue). Upper left shows
601 the 3D shapes of trapped gas bubbles with a different color assigned to different gas bubbles.

602

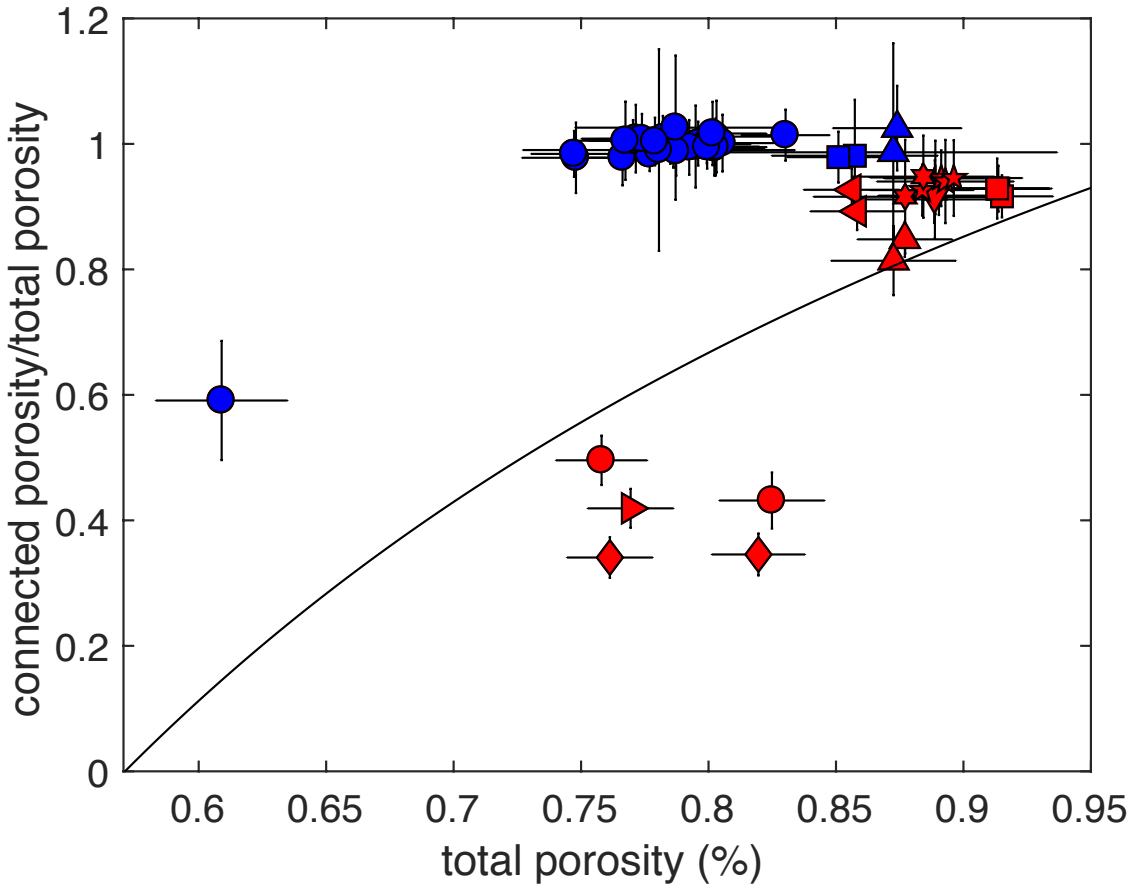

Figure 4: Connected fraction of total porosity vs. total porosity for seafloor giant pumice samples (blue) and raft samples (red). The measurements were conducted on multiple cores from three seafloor giant pumice samples and nine raft samples. Distinct samples are shown with different symbols. Excluding one seafloor measurement, which was collected from a breadcrusted exterior, the seafloor giant pumice samples all have > 99% connected porosity. All raft samples contain isolated vesicles. Shown with the curve is the amount of connected porosity needed, as a function of total porosity to allow clasts to sink if the connected pore space fills completely with water (equation B.9).

614

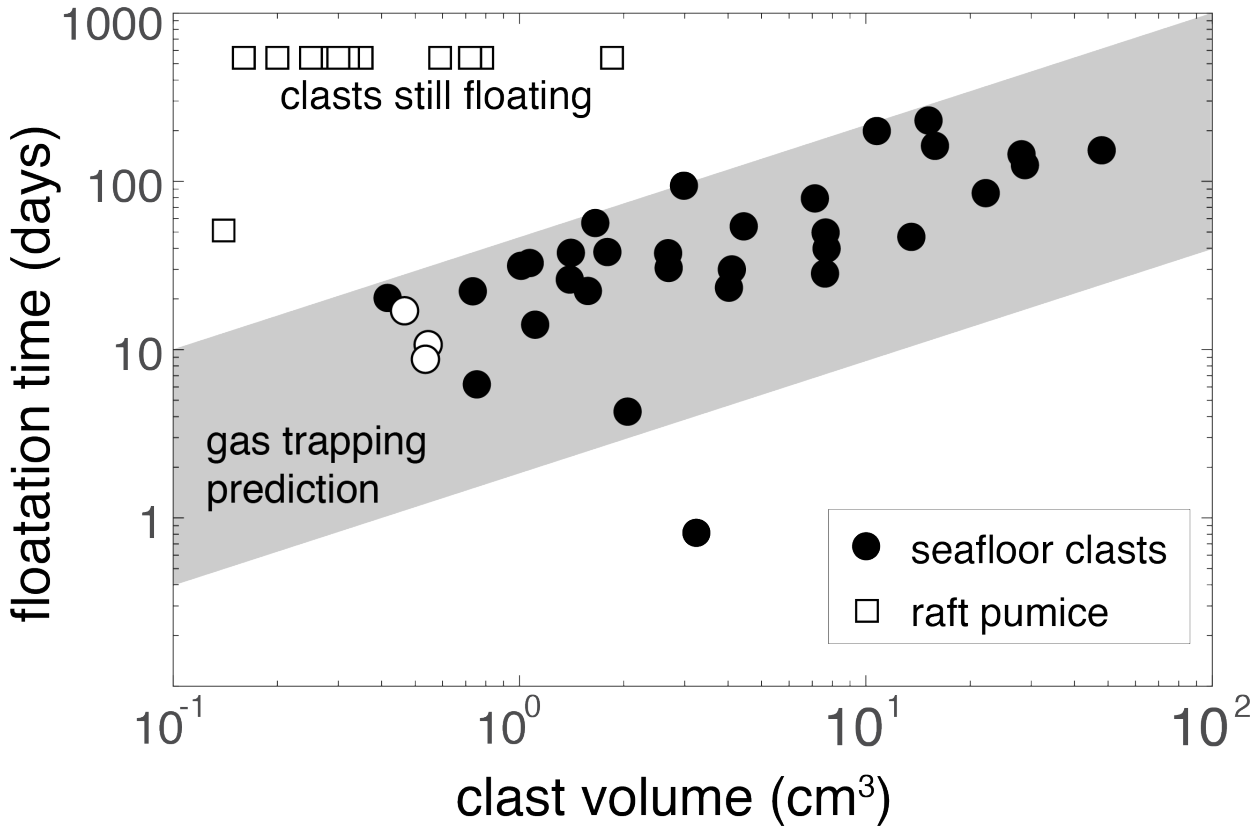

615

616 **Figure 5**: Clast volume versus floatation time (the time at which clasts sink). Data points above
617 "still floating" show clasts that were still floating at the time of manuscript submission. Open
618 data points represent clasts for which volume was calculated from weight and by assuming
619 porosity; black data points represent clasts for which volume was measured using
620 photogrammetry. From calculated porosity from mass and volume measurements we find that
621 seafloor clasts have porosities of 85.6±3.2%. The grey bar represents a floatation time prediction
622 from equation (2) and assuming $0.1 < \theta < 0.5$. The behavior of seafloor clasts matches the gas
623 trapping prediction while that of raft clasts does not. Error bars are smaller than the data points.

624

625

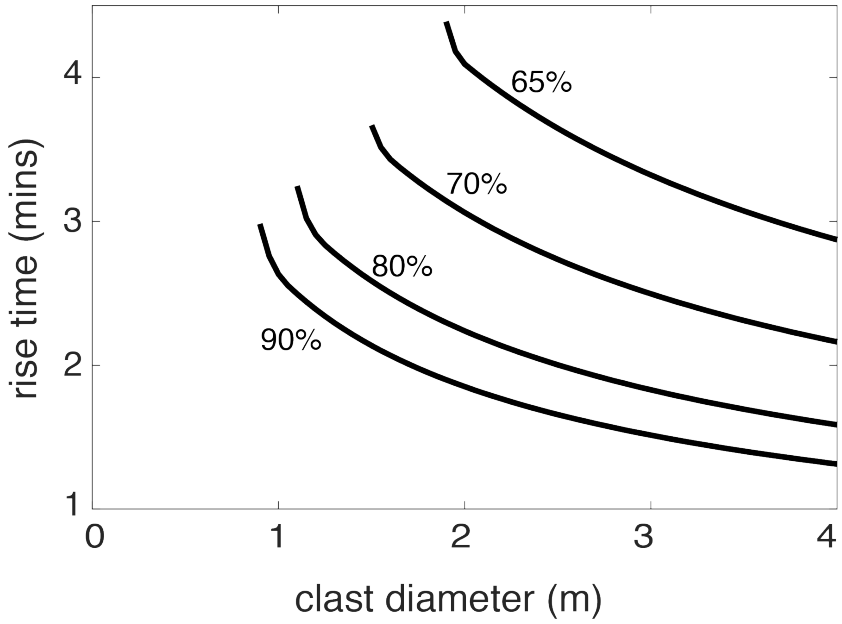

626

627

628 **Figure 6**: Time required for clasts to reach the ocean surface from a depth of 900 m as a function
629 of their size and vesicularity (assumed constant during ascent). Clasts with diameters smaller
630 than those for which the curves begin (to the left of the curves) will ingest enough water to
631 become negatively buoyant before reaching the surface. Rise speed evolves according to
632 equation (2) and clast density is computed from the water ingestion model (appendix B).

633

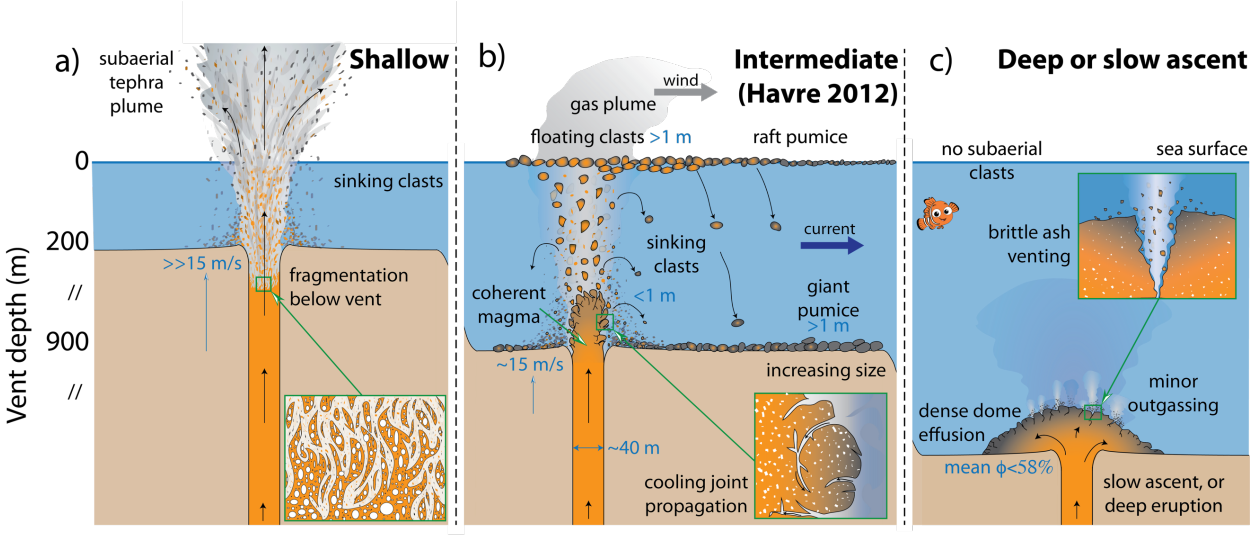

Figure 7: Schematic illustration of the eruption of magma with Havre composition and water content, but at different depths: a) shallow enough that fragmentation occurs in the conduit, b) Havre vent depth, and c) deep or ascended slow enough that vesicularity is < 58%. In b), clast size in the raft decreases with transport owing to abrasion. Inset in each panel illustrates the manner in which clasts might form, either within the conduit (a), or quenching in water (b and c). Panel b) illustrates the settling of smaller clasts close to the vent, the rise of large, hot clasts to the sea surface, the trapping of hot pumice beneath the sea surface, and the settling of giant pumice out of the raft due to water ingestion. The relative temperature gradient of melt to glass in clasts given from orange to grey, respectively. White shapes are vesicles. Liquid water is blue. Not to scale.

646

647

648 **References cited**

649

650 Allen, R. L., Weihed, P., & Svenson, S. A. (1996). Setting of Zn-Cu-Au-Ag massive sulfide
651 deposits in the evolution and facies architecture of a 1.9 Ga marine volcanic arc, Skellefte
652 District, Sweden. *Economic Geology*, *91*(6), 1022-1053.

653

654 Allen, S. R., Fiske, R. S., & Cashman, K. V. (2008). Quenching of steam-charged pumice:
655 Implications for submarine pyroclastic volcanism. *Earth and Planetary Science Letters*, *274*(1),
656 40-49.

657

658 Allen, S. R., & McPhie, J. (2009). Products of neptunian eruptions. *Geology*, *37*(7), 639-642.

659

660 Allen, S. R., Fiske, R. S., & Tamura, Y. (2010). Effects of water depth on pumice formation in
661 submarine domes at Sumisu, Izu-Bonin arc, western Pacific. *Geology*, *38*(5), 391-394.

662

663 Bagdassarov, N., & Dingwell, D. (1994). Thermal properties of vesicular rhyolite. *Journal of*
664 *Volcanology and Geothermal Research*, *60*(2), 179-191.

665

666 Bredehoeft, J. D., & Papaopulos, I. S. (1965). Rates of vertical groundwater movement estimated
667 from the Earth's thermal profile. *Water Resources Research*, *1*(2), 325-328.

668

669 Barker, S. J., Rotella, M. D., Wilson, C. J., Wright, I. C., & Wysoczanski, R. J. (2012).
670 Contrasting pyroclast density spectra from subaerial and submarine silicic eruptions in the
671 Kermadec arc: implications for eruption processes and dredge sampling. *Bulletin of*
672 *volcanology*, *74*(6), 1425-1443.
673
674 Batchelor, G. K. (1967). An Introduction to Fluid Mechanics, 615 pp. *Cambridge University*
675 *Press, New York*.
676
677 Burgisser, A., Chevalier, L., Gardner, J. E., & Castro, J. M. (2017). The percolation threshold
678 and permeability evolution of ascending magmas. *Earth and Planetary Science Letters*, *470*, 37-
679 47.
680
681 Carey, R. J., Wysoczanski, R., Wunderman, R., & Jutzeler, M. (2014). Discovery of the largest
682 historic silicic submarine eruption. *Eos, Transactions American Geophysical Union*, *95*(19), 157-
683 159.
684
685 Carey, R., Soule, S. A., Manga, M., White, J., McPhie, J., Wysoczanski, R., ... & Caratori-
686 Tontini, F. (2018). The largest deep-ocean silicic volcanic eruption of the past century. *Science*
687 *Advances*, *4*(1), e1701121.
688
689 Cas, R. A. F., & Wright, J. V. (1987). Volcanic Successions, Modern and Ancient: A Geological
690 Approach to Processes, Products and Successions, 528 pp.
691

692 Cas, R. A., & Giordano, G. (2014). Submarine volcanism: a review of the constraints, processes
693 and products, and relevance to the Cabo de Gata volcanic succession. *Italian Journal of*
694 *Geosciences*, *133*(3), 362-377.
695
696 Cashman, K. V., & Fiske, R. S. (1991). Fallout of pyroclastic debris from submarine volcanic
697 eruptions. *Science(Washington)*, *253*(5017), 275-280.
698
699 Colombier, M., Wadsworth, F. B., Gurioli, L., Scheu, B., Kueppers, U., Di Muro, A., &
700 Dingwell, D. B. (2017). The evolution of pore connectivity in volcanic rocks. *Earth and*
701 *Planetary Science Letters*, *462*, 99-109.
702
703 Costa, A. (2005). Viscosity of high crystal content melts: dependence on solid
704 fraction. *Geophysical Research Letters*, *32*(22).
705
706 Degruyter, W., Bachmann, O., Burgisser, A., & Manga, M. (2012). The effects of outgassing on
707 the transition between effusive and explosive silicic eruptions. *Earth and Planetary Science*
708 *Letters*, *349*, 161-170.
709
710 Dufek, J., Manga, M., & Staedter, M. (2007). Littoral blasts: Pumice-water heat transfer and the
711 conditions for steam explosions when pyroclastic flows enter the ocean. *Journal of Geophysical*
712 *Research: Solid Earth*, *112*(B11).
713
714 Fauria, K. (2017) PhD dissertation, University of California, Berkeley.

715

716 Fauria, K. E., Manga, M., & Wei, Z. (2017). Trapped bubbles keep pumice afloat and gas
717 diffusion makes pumice sink. *Earth and Planetary Science Letters*, *460*, 50-59.

718

719 Giachetti, T., Druitt, T. H., Burgisser, A., Arbaret, L., & Galven, C. (2010). Bubble nucleation,
720 growth and coalescence during the 1997 Vulcanian explosions of Soufrière Hills Volcano,
721 Montserrat. *Journal of Volcanology and Geothermal Research*, *193*(3), 215-231.

722

723 Giordano, D., Russell, J. K., & Dingwell, D. B. (2008). Viscosity of magmatic liquids: a
724 model. *Earth and Planetary Science Letters*, *271*(1), 123-134.

725

726 Gonnermann, H. M., & Manga, M. (2005). Nonequilibrium magma degassing: results from
727 modeling of the ca. 1340 AD eruption of Mono Craters, California. *Earth and Planetary Science*
728 *Letters*, *238*(1), 1-16.

729

730 Gonnermann, H., Giachetti, T., Nguyen, C. T., Houghton, B. F., Crozier, J. A., & Carey, R. J
731 (2017). Permeability during magma expansion and compaction. *Journal of Geophysical*
732 *Research: Solid Earth*.

733

734 Holmgren, M. (2006). X Steam for Matlab. *www. x-eng. com, accessed November*, *20*, 2017.

735

736 Houghton, B.F., Hobden, B.J., Cashman, K.V., Wilson, C.J.N. and Smith, R.T. (2003). Large-
737 Scale Interaction of Lake Water and Rhyolitic Magma During the 1.8 Ka Taupo Eruption, New
738 Zealand. Explosive subaqueous volcanism, pp. 97-109.
739
740 Jutzeler, M., Marsh, R., Carey, R. J., White, J. D., Talling, P. J., & Karlstrom, L. (2014). On the
741 fate of pumice rafts formed during the 2012 Havre submarine eruption. *Nature*
742 *communications*, *5*.
743
744 Jutzeler, M., Manga, M., White, J. D. L., Talling, P. J., Proussevitch, A. A., Watt, S. F. L.,
745 Cassidy, R.N., Le Friant, A., & Ishizuka, O. (2017). Submarine deposits from pumiceous
746 pyroclastic density currents traveling over water: An outstanding example from offshore
747 Montserrat (IODP 340). *Geological Society of America Bulletin*, *129*(3-4), 392-414.
748
749 Kano, K. (2003). Subaqueous pumice eruptions and their products: A review. *Explosive*
750 *subaqueous volcanism*, 213-229.
751
752 Kano, K., Yamamoto, T., & Ono, K. (1996). Subaqueous eruption and emplacement of the
753 Shinjima Pumice, Shinjima (Moeshima) Island, Kagoshima Bay, SW Japan. *Journal of*
754 *Volcanology and Geothermal Research*, *71*(2-4), 187-206.
755
756 Y. Kato, Y. (1987). Woody pumice generated with submarine eruption. *Journal of the*
757 *Geological Society of Japan, 93*, 11-20 (1987).
758

759 Kozono, T., & Koyaguchi, T. (2009). Effects of relative motion between gas and liquid on 1-
760 dimensional steady flow in silicic volcanic conduits: 2. Origin of diversity of eruption
761 styles. *Journal of Volcanology and Geothermal Research*, *180*(1), 37-49.
762
763 Kueppers, U., Nichols, A.R.L., Zanon, V., Potuzak, M., and Pacheco, J.M.R. (2012). Lava
764 balloons – peculiar products of basaltic submarine eruptions. *Bulletin of Volcanology, 74*, 1379-
765 1393.
766
767 Llewellin, E. W., & Manga, M. (2005). Bubble suspension rheology and implications for conduit
768 flow. *Journal of Volcanology and Geothermal Research*, *143*(1), 205-217.
769
770 Manville, V., White, J. D. L., Houghton, B. F., & Wilson, C. J. N. (1998). The saturation
771 behaviour of pumice and some sedimentological implications. *Sedimentary Geology*, *119*(1), 5-
772 16.
773
774 McPhie, J., & Allen, R. L. (2003). Submarine, Silicic, Syn-Eruptive Pyroclastic Units in the
775 Mount Read Volcanics, Western Tasmania: Influence of Vent Setting and Proximity on
776 Lithofacies Characteristics. *Explosive Subaqueous Volcanism*, 245-258.
777
778 Mitchell, S. J., McIntosh, I. M., Houghton, B. F., Carey, R. J., & Shea, T., (in review). Dynamics
779 of a powerful deep submarine eruption recorded in H2O contents and speciation in rhyolitic
780 glass: The 2012 Havre eruption, *Earth and Planetary Science Letters*
781

Mueller, S., Melnik, O., Spieler, O., Scheu, B., & Dingwell, D. B. (2005). Permeability and degassing of dome lavas undergoing rapid decompression: an experimental determination. *Bulletin of Volcanology*, *67*(6), 526-538.

National Academies of Sciences, Engineering and Medicine (2017). Volcanic eruptions and their repose, unrest, precursors, and time. Washington, DC: The National Academies Press. https://doi.org/10.17226/24650.

Olson, P., & Singer, H. (1985). Creeping plumes. *Journal of Fluid Mechanics*, *158*, 511-531.

Papale, P. (1999). Strain-induced magma fragmentation in explosive eruptions. *Nature*, *397*(6718), 425-428.

Putirka, K. D. (2008). Thermometers and barometers for volcanic systems. *Reviews in Mineralogy and Geochemistry*, *69*(1), 61-120.

Randolph-Flagg, N., Breen, S., Hernandez, A., Manga, M., & Self, S. (2017). Evenly spaced columns in the Bishop Tuff (California, USA) as relicts of hydrothermal cooling. *Geology*, *45*(11), 1015-1018.

Reynolds, M. A., Best, J. G., & Johnson, R. W. (1980). *1953-57 Eruption of Tuluman Volcano: Rhyolitic Volcanic Activity in the Northern Bismarck Sea* (Vol. 7). Geological Survey of Papua New Guinea.

Risso, C., Scasso, R. A., & Aparicio, A. (2002). Presence of large pumice blocks on Tierra del Fuego and South Shetland Islands shorelines, from 1962 South Sandwich Islands eruption. *Marine Geology*, *186*(3), 413-422.

Rotella, M. D., Wilson, C. J., Barker, S. J., & Wright, I. C. (2013). Highly vesicular pumice generated by buoyant detachment of magma in subaqueous volcanism. *Nature Geoscience*, *6*(2), 129.

Rotella, M. D., Wilson, C. J., Barker, S. J., Schipper, C. I., Wright, I. C., & Wysoczanski, R. J. (2015). Dynamics of deep submarine silicic explosive eruptions in the Kermadec arc, as reflected in pumice vesicularity textures. *Journal of Volcanology and Geothermal Research*, *301*, 314-332.

Rust, A. C., & Cashman, K. V. (2004). Permeability of vesicular silicic magma: inertial and hysteresis effects. *Earth and Planetary Science Letters*, *228*(1), 93-107.

Shea, T., Hammer, J., & First, E. (2013). Magma balloons or bombs? *Nature Geoscience*, *6*(10), 802-803.

Simmons, J. H. (1998). What is so exciting about non-linear viscous flow in glass, molecular dynamics simulations of brittle fracture and semiconductor–glass quantum composites. *Journal of non-crystalline solids*, *239*(1), 1-15.

828

829 Vella, D., & Huppert, H. E. (2007). The waterlogging of floating objects. *Journal of Fluid*
830 *Mechanics*, *585*, 245-254.

831

832 van Otterloo, J., Cas, R. A., & Scutter, C. R. (2015). The fracture behaviour of volcanic glass and
833 relevance to quench fragmentation during formation of hyaloclastite and
834 phreatomagmatism. *Earth-Science Reviews*, *151*, 79-116.

835

836 von Lichtan, I. J., White, J. D. L., Manville, V., & Ohneiser, C. (2016). Giant rafted pumice
837 blocks from the most recent eruption of Taupo volcano, New Zealand: Insights from
838 palaeomagnetic and textural data. *Journal of Volcanology and Geothermal Research*, *318*, 73-88.

839

840 White, J.D., Schipper, C.I. and Kano, K. (2015). Submarine explosive eruptions. In *The*
841 *Encyclopedia of Volcanoes (Second Edition)* (pp. 553-569).

842

843 Whitham, A. G., & Sparks, R. S. J. (1986). Pumice. *Bulletin of Volcanology*, *48*(4), 209-223.

844

845 Wilson, C. J. N., & Walker, G. P. (1985). The Taupo eruption, New Zealand I. General
846 aspects. *Philosophical Transactions of the Royal Society of London A: Mathematical, Physical*
847 *and Engineering Sciences*, *314*(1529), 199-228.

848 Wright, H., Roberts, J.J. and Cashman, K.V., 2006. Permeability of anisotropic tube pumice:
849 Model calculations and measurements. *Geophysical research letters*, *33*(17).

850

S1 Conduit model parameters

Magma ascent is modeled assuming steady isothermal two-phase flow in a cylindrical conduit with constant radius. The flow is one-dimensional with all properties varying only with depth. The equations solved are identical to those in Degruyter et al. (2012) with fragmentation criterion given by (1) and a few modifications. We fit a model for melt viscosity with the same functional form as that in Hess and Dingwell (1996) with viscosity computed from Giordano et al. (2008) and measured composition (S3),

$$\log \mu = -3.62517 + 0.248398 \ln(100c) + \frac{9601 - 2368 \ln(100c)}{T - (195.7 + 96.4931 \ln(100c)}$$

where c is the water concentration in mass fraction and T is temperature.

The magma viscosity μ_m is given by

$$\mu_m = \mu(c, T)\theta(\chi)v(\phi)$$

where $\theta(\chi)$ accounts for the effects of crystals (5% assumed) on magma viscosity (Costa, 2005), and

$$v(\phi) = (1 - \phi)^{5/3}$$

accounts for the effects of bubbles (Llewellin and Manga, 2005).

Other parameters used in the model include a gas viscosity of 10^{-5} Pa s, a conduit length of 8100 m, magma temperature of 850 °C, melt density of 2400 kg m^{-3}, initial water content of 5.8 weight %, initial pressure of 200 MPa, vent pressure of 9 MPa, bubble number density of 10^{14} m^{-3}, tortuosity factor m of 3, friction factor f_0 of 10, a throat/bubble size ratio f_{tb} of 0.3125, and a percolation threshold of 0 (continuous percolation).

References for S1

Costa, A. (2005). Viscosity of high crystal content melts: dependence on solid fraction. *Geophysical Research Letters*, *32*(22).

Degruyter, W., Bachmann, O., Burgisser, A., & Manga, M. (2012). The effects of outgassing on the transition between effusive and explosive silicic eruptions. *Earth and Planetary Science Letters*, *349*, 161-170.

Giordano, D., Russell, J. K., & Dingwell, D. B. (2008). Viscosity of magmatic liquids: a model. *Earth and Planetary Science Letters*, *271*(1), 123-134.

Hess, K. U., & Dingwell, D. D. (1996). Viscosities of hydrous leucogranitic melts: A non-Arrhenian model. *American Mineralogist*, *81*(9-10), 1297-1300.

Llewellin, E. W., & Manga, M. (2005). Bubble suspension rheology and implications for conduit flow. *Journal of Volcanology and Geothermal Research*, *143*(1), 205-217.

887 **S2 Initial water content**

888

889 Initial dissolved volatile contents *c* were measured using the CAMECA IMS 1280 secondary ion
890 mass spectrometer at Woods Hole Oceanographic Institution, Massachusetts. H_2O, CO_2 and F
891 contents were obtained from 16 plagioclase-hosted melt inclusions from a giant pumice block
892 retrieved from the seafloor (Carey et al., in press). Melt inclusions analyzed ed had no visible
893 fractures or pathways to the phenocryst edge and no vapor bubbles present.

894

895 Raw $^{16}O^{1}H/^{30}Si$ ratios from the SIMS were calibrated to H_2O wt % using calibration curves
896 determined from a series of rhyolite standards and synthetic forsterite with known FTIR H_2O wt
897 %. Likewise, CO_2 and F were determined using the raw $^{12}C/^{30}Si$ and $^{35}F/^{30}Si$ ratios from the
898 samples and known CO_2 and F calibration curves from the standards. Measurements are
899 summarized in Table S2.1.

900

901 H_2O and F contents were used in the initial melt viscosity calculation (supplement S1); F
902 contents <0.1 wt % (1000 ppm) had a negligible effect on viscosity. Figure S2.1 shows that H_2O
903 and CO_2 contents were also used to determine the initial model pressure of 200 MPa using the
904 VolatileCalc solubility model (Newman and Lowenstern, 2002). H_2O-CO_2 isobars were
905 determined for a rhyolitic melt at 850°C where all melt inclusions correspond to an average
906 storage pressure of 200 MPa. The very low CO_2 contents (<150 ppm) justifies the use of only
907 H_2O as the volatile phase within the conduit ascent model (S1).

908

909

910 **Table S2.1** Measured volatile contents in melt inclusions of seafloor pumice clasts

911

SIMS data	H_2O (wt %)	CO_2 (ppm)	F (ppm)
Havre melt	5.74	22.8	963
inclusions	6.12	53.9	992
	5.66	124.3	955
	5.07	73.3	888
	6.85	8.8	970
	5.29	77.5	838
	5.83	58.6	996
	5.90	125.2	985
	5.83	33.0	966
	6.38	116.7	1040
	6.48	108.7	1054
	5.58	172.1	935
	5.61	127.9	931
	5.85	21.8	978
	5.81	36.5	901
	5.18	144.1	1022
Average	5.82	81.6	963

912

913

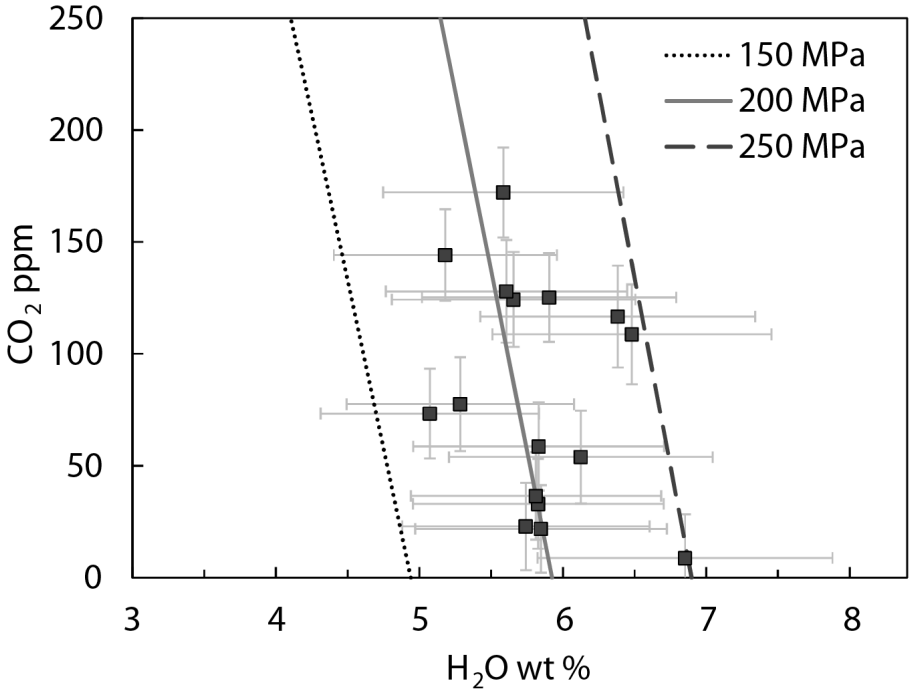

914

915 **Figure S2.1** Measured CO_2 and H_2O in plagioclase-hosted melt inclusions with H_2O-CO_2

916 isobars were determined for a rhyolitic melt at 850°C.

917

918 References for S2

919

920 Newman, S., & Lowenstern, J. B. (2002). VolatileCalc: a silicate melt–H_2O–CO_2 solution model written in Visual

921 Basic for Excel. *Computers & Geosciences*, *28*(5), 597-604.

922

S3 Melt composition

XRF data given in Table S3.1 are the average for 5 giant pumiceous blocks sampled from the seafloor. Values match very well with those from Carey et al. (in press) and Rotella et al., (2015). Fe_2O_3 is corrected to FeO_t for use in the viscosity model (supplement S1).

We assume the initial melt composition is the same as the whole rock plus dissolved water.

Table S3.1 Whole rock composition.

SiO_2	TiO_2	Al_2O_3	FeO_t	MnO	MgO	CaO	Na_2O	K_2O	P_2O_5	Total	LOI
72.437	0.479	14.145	3.017	0.122	0.727	2.608	5.117	1.590	0.083	100.325	1.131

S4 X-ray computed microtomography

X-ray microtomography was performed on beamline 8.3.2 at the Advanced Light Source, Lawrence Berkeley National Lab. We used 30 kev monochromatic x-rays, a 5X lens to obtain a voxel size of 1.22 microns, and used 1024 images and the TomoPy gridrec algorithm (Gursoy et al., 2014) to create the 3D images.

To segment the 3D images into water, gas and glass, we used the Fiji trainable Weka segmentation algorithm (Hall et al., 2009) by manually outlining gas, liquid and glass and retraining the classifiers until the segmentation seemed accurate. The volume fraction of each phase was computed from the binary segmented images in Fiji. Aviso was used to make the images in Figure 4 and to identify distinct bubbles in the 3D rendering.

945

946 References cited in S4

947

948 Gürsoy, D., De Carlo, F., Xiao, X., & Jacobsen, C. (2014). TomoPy: a framework for the analysis of synchrotron
949 tomographic data. *Journal of synchrotron radiation*, *21*(5), 1188-1193.
950 Hall, M., Frank, E., Holmes, G., Pfahringer, B., Reutemann, P., & Witten, I. H. (2009). The WEKA data mining
951 software: an update. *ACM SIGKDD explorations newsletter*, *11*(1), 10-18.

952

953

Supplement S5: Pumice floatation experiments

The seafloor clasts used here were fragments from decimeter pumiceous Havre seafloor samples HVR 020 and HVR 022 (Figure S5.1). We do not distinguish between HVR 020 and HVR 022 in our experiments because these two samples were mixed together when we retrieved them. The raft pumice was provided by Melissa Rotella from samples collected in New Zealand (Rotella et al., 2015), and the clasts we used were rounded by abrasion in the raft. These are different clasts than those used for the connected porosity measurements in Figure 4.

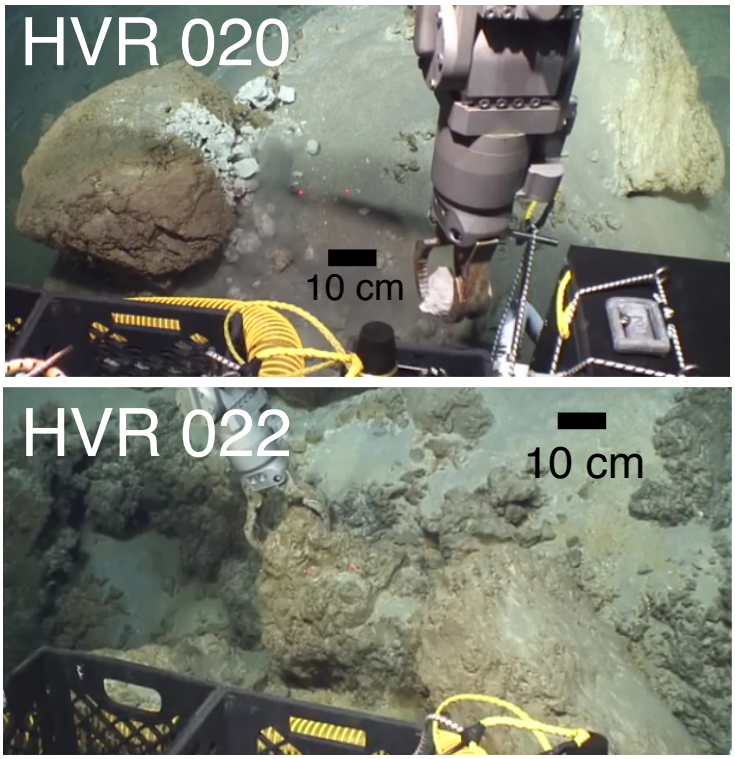

Figure S5.1: Havre seafloor clasts used in the pumice floatation experiments. HVR 020 and HVR 022 are both decimeter pumiceous clasts. The images show the clasts at the time of sample collection (Carey et al., in press).

967

968

969

970 **Table S5.1** Experimental results and measurements of pumice floatation time. * refers to values

971 that were calculated assuming a clast porosity of 83% and "nd" means not directly measured.

pumice name	type	weight (g)	volume (cm^3)	porosity	floatation time (days)
MDR_01	raft	0.058	*0.14	nd	51.03
MDR_02	raft	0.141	*0.35	nd	> 532
MDR_03	raft	0.132	*0.32	nd	> 532
MDR_04	raft	0.064	*0.16	nd	> 532
MDR_05	raft	0.116	*0.28	nd	> 532
MDR_06	raft	0.082	*0.20	nd	> 532
S1_07	raft	0.755	*1.85	nd	> 532
S1_08	raft	0.319	*0.78	nd	> 532
S1_09	raft	0.241	*0.59	nd	> 532
S1_10	raft	0.292	*0.72	nd	> 532
S1_11	raft	0.121	*0.30	nd	> 532
S1_12	raft	0.294	*0.72	nd	> 532
S1_13	raft	0.1	*0.25	nd	> 532
S1_14	raft	0.034	*0.08	nd	> 532
HVR 001	seafloor	1.646	4.14	0.83	29.4
HVR 002	seafloor	1.048	2.71	0.84	36.7
HVR 003	seafloor	0.71	2.07	0.86	4.2
HVR 004	seafloor	0.238	1.02	0.90	30.9
HVR 005	seafloor	0.646	1.67	0.84	55.5
HVR 006	seafloor	0.647	1.59	0.83	21.9
HVR 007	seafloor	0.177	0.42	0.82	19.9
HVR 008	seafloor	0.349	1.08	0.87	32.1
HVR 009	seafloor	0.567	1.41	0.83	25.6
HVR 010	seafloor	0.404	0.76	0.78	6.1

HVR 011	seafloor	0.446	1.42	0.87	36.9
HVR 012	seafloor	0.249	0.74	0.86	21.8
HVR 013	seafloor	0.423	1.12	0.84	13.8
HVR 015	seafloor	0.905	3.01	0.88	92.5
HVR 016	seafloor	0.228	0.54	0.83	8.6
HVR 017	seafloor	0.192	*0.47	nd	16.7
HVR 018	seafloor	1.747	3.27	0.78	0.8
HVR 018	seafloor	1.747	3.27	0.78	0.8
HVR 019	seafloor	0.539	1.81	0.88	37.3
HVR 020	seafloor	0.925	2.72	0.86	30
HVR 021	seafloor	5.465	15.97	0.86	159.5
HVR 022	seafloor	9.931	22.38	0.82	83.5
HVR 023	seafloor	14.601	29.04	0.79	122.5
HVR 024	seafloor	22.521	48.37	0.81	150.1
HVR 025	seafloor	0.224	*0.55	nd	10.5
HVR 026	seafloor	11.432	28.39	0.83	142.1
HVR 028	seafloor	6.632	13.65	0.80	45.9
HVR 030	seafloor	0.222	*0.54	nd	8.6
HVR 031	seafloor	5.481	15.30	0.85	225.6
HVR 032	seafloor	4.121	7.72	0.78	48.7
HVR 033	seafloor	1.461	4.06	0.85	22.9
HVR 034	seafloor	2.252	4.48	0.79	53
HVR 035	seafloor	2.817	7.19	0.84	77.7
HVR 036	seafloor	3.648	10.85	0.86	195.5
HVR 037	seafloor	3.69	7.77	0.80	39.1
HVR 038	seafloor	2.803	7.69	0.85	27.8

972